J Mater Sci (2009) 44:808–815
DOI 10.1007/s10853-008-3148-2

Intra-granular alpha precipitation in Ti–Nb–Zr–Ta biomedical alloys

S. Nag · R. Banerjee · H. L. Fraser

Received: 24 November 2008 / Accepted: 1 December 2008 / Published online: 27 December 2008

Abstract This article investigates the intra-granular precipitation of nanometer-scale α platelets in the β matrix of a complex quaternary β titanium alloy, Ti-35Nb-7Zr-5Ta (all in wt%), for orthopedic implant applications, during β-solutionizing/quenching/aging type heat-treatments. The role of metastable ω precipitates on the nucleation and growth of these α precipitates, has been specifically addressed by coupling transmission electron microscopy (TEM) and 3D atom probe (3DAP) tomography studies on this alloy. Athermal ω precipitates form in this alloy on quenching from above the β-transus temperature. On isothermal annealing at low temperatures ($\sim$400 °C), these ω precipitates coarsen, rejecting Zr into the adjacent β matrix as determined by 3DAP studies. Concurrently, the nucleation and growth of α precipitates is initiated at or near the ω/β interfaces, as determined by TEM studies. In addition to coherency strains induced by the ω precipitates, the local enrichment of Zr adjacent to these precipitates appears to play an important role in aiding the nucleation and growth of Zr-rich α precipitates in this alloy.

Introduction

β titanium alloys have applications in a number of different areas including aerospace (e.g., airframes and aircraft landing gear) and biomedical (e.g., orthopedic and dental implants). Due to the rapidly increasing number of surgical procedures involving prosthesis implantation there is an urgent need for improved biomaterials and processing technologies for orthopedic implants such as hip implants. Since the β phase in Ti alloys exhibits a significantly lower modulus than the α phase leading to reduced stress-shielding problems [1, 2], and the β alloys also satisfy most of the other requirements for an ideal orthopedic alloy, there is a thrust towards the development of lower modulus β-Ti alloys which retain a single β phase microstructure on rapidly cooling from high temperatures. Two recently developed promising biomedical alloys, Ti-35Nb-7Zr-5Ta (all in wt%, referred in short as TNZT) [3] and Ti-29Nb-13Ta-4.6Zr [4], show significant improvements in these aspects compared to previous generation alloys such as Ti-6Al-4 V, stainless-steel, and cobalt–chromium-based ones. Furthermore, since these implants are geometrically quite complex and have different property requirements at different locations, their manufacturing becomes particularly challenging. By employing novel near-net shape processing technologies, such as laser-engineered net shaping (LENS$^{\text{TM}}$) [5], it is possible to not only rapidly and efficiently manufacture custom-designed implants but also functionally grade them to exhibit required site-specific properties. Recent experiments have demonstrated success in depositing complex homogeneous alloys and metal-matrix composites, including alloys and composites based on Ti–Nb–Zr–Ta, using the LENS$^{\text{TM}}$ process [6, 7].

While a single β phase microstructure exhibits the lowest modulus, lower yield strength corresponding to such

S. Nag (✉) · R. Banerjee
Department of Materials Science and Engineering,
University of North Texas, Denton, TX, USA
e-mail: nag.soumya@gmail.com

H. L. Fraser
Center for the Accelerated Maturation of Materials,
Department of Materials Science and Engineering,
The Ohio State University, Columbus, OH, USA

microstructures can be an issue for these titanium alloys. Therefore, in order to achieve a good balance of mechanical properties in alloys such as Ti-35Nb-7Zr-5Ta, the presence of a certain volume fraction of α might be beneficial [8]. However, the volume fraction, size, morphology, and distribution of α precipitates within the β matrix needs to be appropriately engineered by varying the temperatures, times, and cooling rates in individual heat-treatments. Typically, the nucleation sites for the α phase within the β phase of β titanium alloys include, prior β grain boundaries, β/ω interfaces, β/β' interfaces, and other defects such as dislocations and inclusions within the matrix [9]. Depending on the overall composition of the β titanium alloy and the specific heat-treatment experienced by the alloy, these different sites may or may not play a substantial role in α nucleation. The influence of these various nucleation sites is also closely associated with the competing instabilities inherent within the β phase, i.e., $\beta \rightarrow \beta + \beta'$ (phase separation), $\beta \rightarrow \beta + \omega$, and, $\beta \rightarrow \beta + \alpha'$. Typically, in β alloys that are solution treated above the β transus temperature and quenched, athermal ω precipitates form, which on subsequent isothermal aging undergo coarsening and act as uniformly distributed heterogeneous nucleation sites for α precipitates [10, 11]. Such ω-mediated nucleation leads to the formation of homogeneously distributed α precipitates of a relatively finer scale (usually nanometers to sub-micron), often exhibiting morphologies that are distinctly different from precipitates nucleated at higher temperatures at prior β grain boundaries. Previous literature indicates that the lattice mismatch between the ω and β strongly influences the role of ω precipitates on the nucleation of α [10]. Titanium base alloy systems exhibiting a larger mismatch between the ω and β phases, form more cuboidal shaped ω precipitates which act as potent nucleation sites for α, e.g., the binary Ti–V system [10, 11]. In contrast, systems exhibiting a lower mismatch between the ω and β phases, such as the Ti–Mo system form more ellipsoidal-like ω precipitates which may not often act as nucleation sites for α [10]. In more recent studies on more complex β alloys such as the Ti-10 V-2Fe-3Al (Ti-10-2-3) alloy, Ohmori et al. [12] have presented evidence of ω precipitates acting as heterogeneous nucleation sites for α precipitates. Interestingly, while these previous studies have to some degree address the issue of ω-mediated nucleation of α, the details of this phase transformation, especially the role of compositional partitioning of alloying elements, has not been discussed. Such compositional partitioning becomes particularly pertinent in case of complex alloys with multiple alloying additions, such as the present TNZT alloy. Therefore, the focus of the present study is not only to investigate the microstructural details of ω-mediated nucleation of α in TNZT based on TEM studies, but also to measure the compositional partitioning of the pertinent alloying elements during this process based on 3D atom probe (3DAP) studies.

Experimental procedure

The TNZT alloys were deposited using the LENS^{TM} process from a blend of elemental Ti, Nb, Zr, and, Ta, powders. The details of the LENS^{TM} process [5] and the specific deposition used for the TNZT alloys can be found elsewhere [6]. The as-deposited specimens were subsequently heat-treated in two steps. The first step consisted of a β solutionizing treatment in which the alloy samples were heated to 1,000 °C (above the β transus temperature for this alloy ~800 °C), held for 30 min, and then quenched in water. This heat-treatment will be subsequently referred to as the β-solutionized and quenched condition in this article. In the second step these β-solutionized samples were further annealed at 400 °C for 2 h and subsequently quenched in water. The LENS^{TM}-deposited samples were characterized post heat-treatment using scanning electron microscopy (SEM), transmission electron microscopy (TEM), and, 3DAP tomography. The SEM studies were carried out in a FEI/Philips XL-30 SEM equipped with a field emission gun (FEG) source and an EDS detector. Sample preparation for TEM studies involved drilling of 3 mm diameter cylinders by Electro-discharge Machining (EDM), followed by sectioning of thin disks from these cylinders which were subsequently mechanically thinned and ion-milled to electron transparency in a Gatan Duo Mill. The TEM specimens were characterized in a Philips CM200 TEM at an operating voltage of 200 keV. The 3DAP tomography studies were carried out in a local electrode atom probe (LEAP^{TM}) microscope system. For LEAP^{TM} analysis, samples were prepared using a dual-beam focused ion beam (FIB), specifically the Nova Nanolab 200 system from FEI. Typically 20 μm × 5 μm × 5 μm sections were extracted from the samples using the Omniprobe^{TM} in the FIB, then mounted onto silicon microtips. The microtip samples consisted of a 6 × 6 array of flat-top silicon micropillars (~5 μm height and ~3 μm flat-plateau diameter) on a 10 mm × 20 mm silicon wafers. On each microtip, final specimens of ~3 μm length and ~70 nm tip diameter were prepared by annular ion milling using the FIB. The details of the sample preparation procedure are described elsewhere [13]. Subsequently, these samples were used for 3DAP tomography studies carried out in LEAP^{TM} microscope. All atom probe experiments were carried out in the electric-field evaporation mode at a temperature of 70 K, with the evaporation rate varied from 0.2 to 1.0% and the pulsing voltage at 20% of the steady-state applied voltage.

Results and discussion

Based the SEM-EDS measurements the nominal composition of the LENS$^{\mathrm{TM}}$-deposited alloy was determined to be Ti-34%Nb-7%Zr-7%Ta (all in wt%). The error associated with the measurement of compositions using EDS in a SEM is typically $\sim$1–2%. In addition, the oxygen contents of these samples, measured using a LECO analyzer was $\sim$0.16 wt%. The microstructure of the LENS$^{\mathrm{TM}}$-deposited TNZT sample, after β solutionizing and quenching, is shown in the bright-field TEM image in Fig. 1a. This image shows a grain boundary between two β grains. A selected area diffraction (SAD) pattern recorded along the [113] β zone axis is shown in Fig. 1b. In this SAD pattern, in addition to the primary reflections arising from the β matrix, secondary precipitate reflections are also visible along the $g = (21\bar{1})\beta$ vector, with sharp spots at the 1/3 and 2/3 $(21\bar{1})\beta$ locations as well as some diffuse intensity at the 1/2 $(21\bar{1})\beta$ locations and other equivalent vectors. While the secondary reflections at the 1/3 and 2/3 $(21\bar{1})\beta$ positions can be attributed to precipitates of the ω phase in the β matrix, the weak diffuse intensity at the 1/2 $(21\bar{1})\beta$ type positions might be the arising from the early stages of α nucleation within the same β matrix [14, 15]. A dark-field TEM image, recorded from one of the ω-reflections at a 1/3 $(21\bar{1})\beta$ type position is shown in Fig. 1c. Nanometer-scale ω precipitates are clearly seen in this dark-field image indicating that in the solutionized and quenched condition, this alloy consist predominantly of a β matrix with homogeneously distributed ω precipitates. Using standard image analysis techniques, the size distribution of these ω precipitates have been measured and a few of these are shown in Fig. 2a. While the specific precipitates measured are shaded (in red) in the dark-field image shown in Fig. 2a, the corresponding measurements for these precipitates are listed in the table shown below. The two-dimensional measurements indicate that most of these ω precipitates are ellipsoidal with the dimensions of the major and minor axes ranging from 2 to 11 nm. The average equivalent diameters of these ω precipitates is $\sim$5 nm. Compositional analysis at the nanometer scale for the as-deposited TNZT sample was carried out using 3DAP in the LEAP$^{\mathrm{TM}}$ microscope. As an example, compositional profiles for Ti, Nb, Zr, and, Ta, as a function of distance along the axis of a cylinder of diameter 2 nm are shown in Fig. 2b. The composition values have been averaged across the diameter of the cylinder for each step of size 0.15 nm along its axis. Compositional fluctuations of small amplitude, such as the one shown in the figure are visible in these profiles. These fluctuations typically corresponded to regions of dimensions $\sim$5 nm enriched in Ti, depleted in Nb, with no substantial changes in the Zr or Ta profiles. Since the amplitude of these changes is $\sim$15 at.% (for Ti

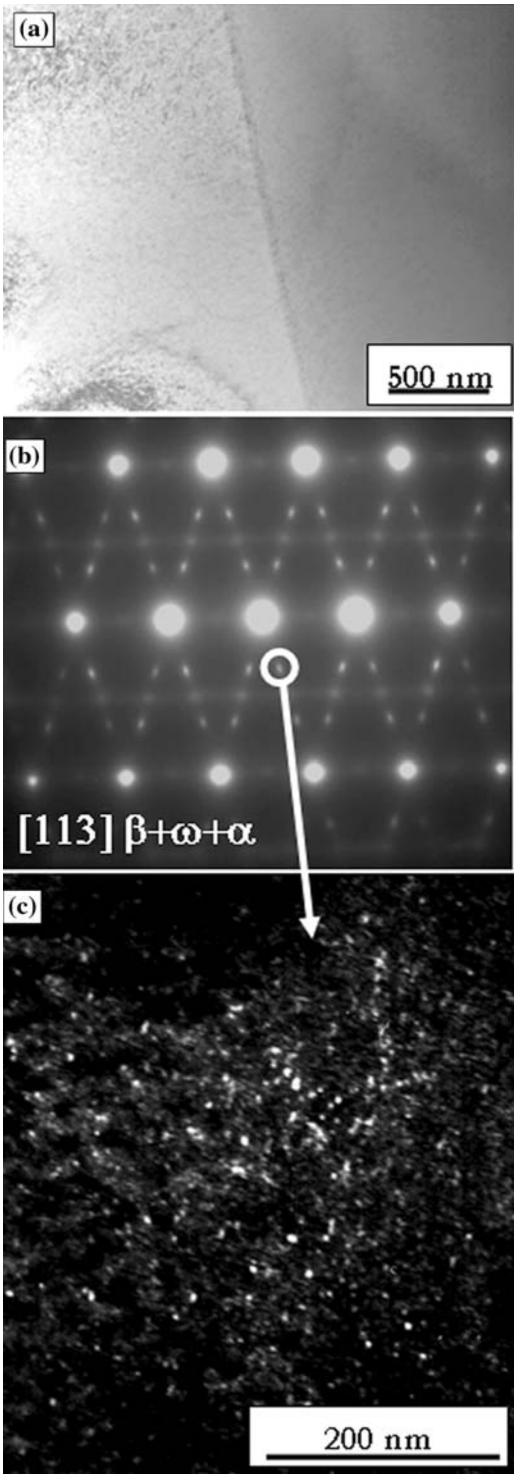

Fig. 1 **a** Bright-field TEM micrograph of β solutionized and quenched LENS$^{\mathrm{TM}}$-deposited TNZT alloy, showing a grain boundary between two primary β grains. **b** [113]β zone axis SAD pattern from the matrix showing sharp spots at the 1/3 and 2/3 $\{112\}\beta$ locations as well as some diffuse intensity at the 1/2 $\{112\}\beta$ locations, corresponding to nanoscale ω and α precipitates, respectively, that are present in this sample. **c** Dark-field TEM image recorded from one of the ω-reflections at a 1/3 $\{112\}\beta$ type position, showing a homogeneous distribution of ω precipitates throughout the matrix

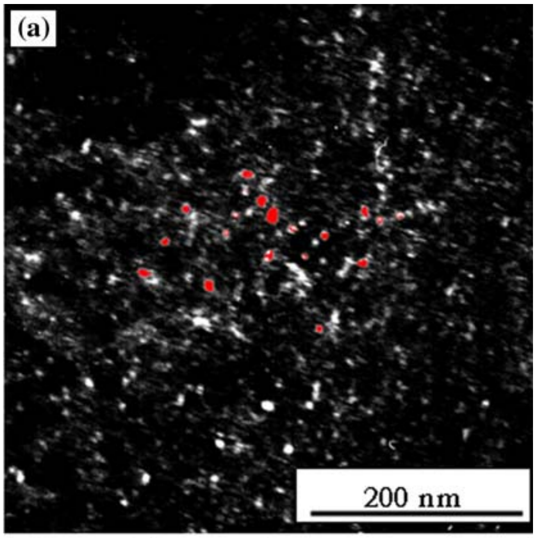

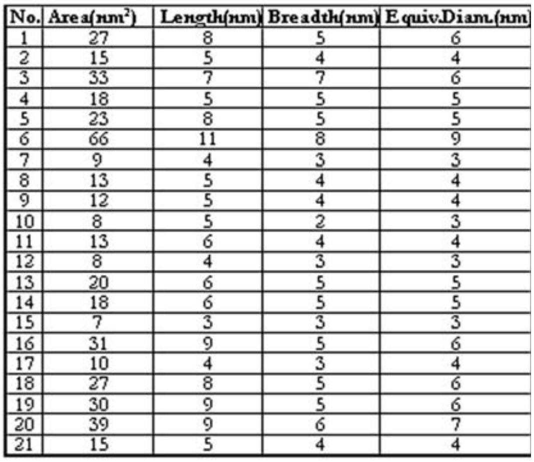

No.	Area(nm^2)	Length(nm)	Breadth(nm)	Equiv.Diam.(nm)
1	27	8	5	6
2	15	5	4	4
3	33	7	7	6
4	18	5	5	5
5	23	8	5	5
6	66	11	8	9
7	9	4	3	3
8	13	5	4	4
9	12	5	4	4
10	8	5	2	3
11	13	6	4	4
12	8	4	3	3
13	20	6	5	5
14	18	6	5	5
15	7	3	3	3
16	31	9	5	6
17	10	4	3	4
18	27	8	5	6
19	30	9	5	6
20	39	9	6	7
21	15	5	4	4

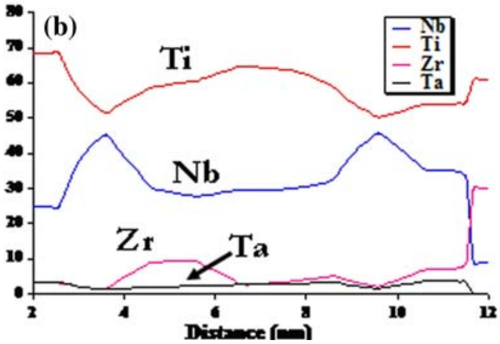

Fig. 2 **a** The same dark-field image as in Fig. 1c where the marked ω particles (in red) are the ones whose sizes were calculated. The table below lists the corresponding values. **b** Compositional variation of a particular ω particle measured via LEAP^{TM} microscope. Here the profiles for Ti, Nb, Zr, and, Ta, as a function of distance along the axis of a cylinder of diameter 2 nm are shown

and Nb), and the samples volume is relatively small, these changes can be partly attributed to statistical noise (hence no error bars were added in this plot). However, since such changes are not uniformly present throughout the analyzed volume in the 3DAP samples coupled with the fact that the dimensions of these compositional fluctuations correspond to the average diameter of ω precipitates (measured from the TEM dark-field images in Fig. 2a), it can be argued that these fluctuations are a consequence of the presence of ω precipitates in the β matrix. From the viewpoint of phase stability, the ω precipitates are expected to exhibit a depletion of Nb (which is a ω de-stabilizer), in concurrence with the experimental observations [16]. However, since these measurements have been carried out in the β-solutionized followed by water-quenched condition of the TNZT alloy, it is unlikely that the fast cooling rate involved will permit any substantial partitioning of the alloying additions between the β and ω phases. This is the main reason behind smaller amplitude changes in Ti and Nb composition plots.

A bright-field TEM image of the TNZT alloy after β solutionizing/quenching/aging at 400 °C for 2 h, is shown in Fig. 3a. In addition to the β matrix phase, nanometer-scale second phase precipitates are clearly visible in this bright-field image. SAD patterns corresponding to the [011] β and [113] β zone axes are shown in Fig. 3b and c, respectively. In both these diffraction patterns, in addition to the primary reflections corresponding to the β phase, additional reflections are clearly visible at the 1/3 and 2/3 {112} β as well as at the 1/2 {112} β locations. As discussed previously, while the reflections at the 1/3 and 2/3 {112} β locations can be attributed to the ω phase, the reflection at the 1/2 {112} β location can be attributed to the α phase. Furthermore, the relatively sharp intensity maxima at the 1/2 {112} β locations indicates that the α precipitates are well-developed in the 400 °C annealed TNZT sample as confirmed by the dark-field TEM micrograph shown in Fig. 3d, recorded from one of these α reflections. These α precipitates exhibit an acicular morphology (based on the two-dimensional TEM images) with lengths of ~tens of nanometers and are a few nanometers wide. A dark-field micrograph, recorded from one of the ω reflections, is shown in Fig. 3e. Well-developed, lenticular-shaped ω precipitates are visible in this image. While these two dark-field images show the individual α and ω precipitates quite clearly, for studying the influence of ω on α nucleation it would be quite useful to image both types of precipitates simultaneously. This can be accomplished by using a larger size objective aperture to include multiple α and ω reflections, such as shown in Fig. 4a, for the [113] β zone axis SAD pattern. The corresponding dark-field image is shown in Fig. 4b, with both α and ω precipitates simultaneously imaged under this condition. In many instances in this dark-field image, the α precipitates appear to be associated with the ω precipitates. A specific example of one such case is taken up in the magnified view shown in Fig. 4c, where an acicular α precipitate appears to be attached to a ω precipitate. Such an association between

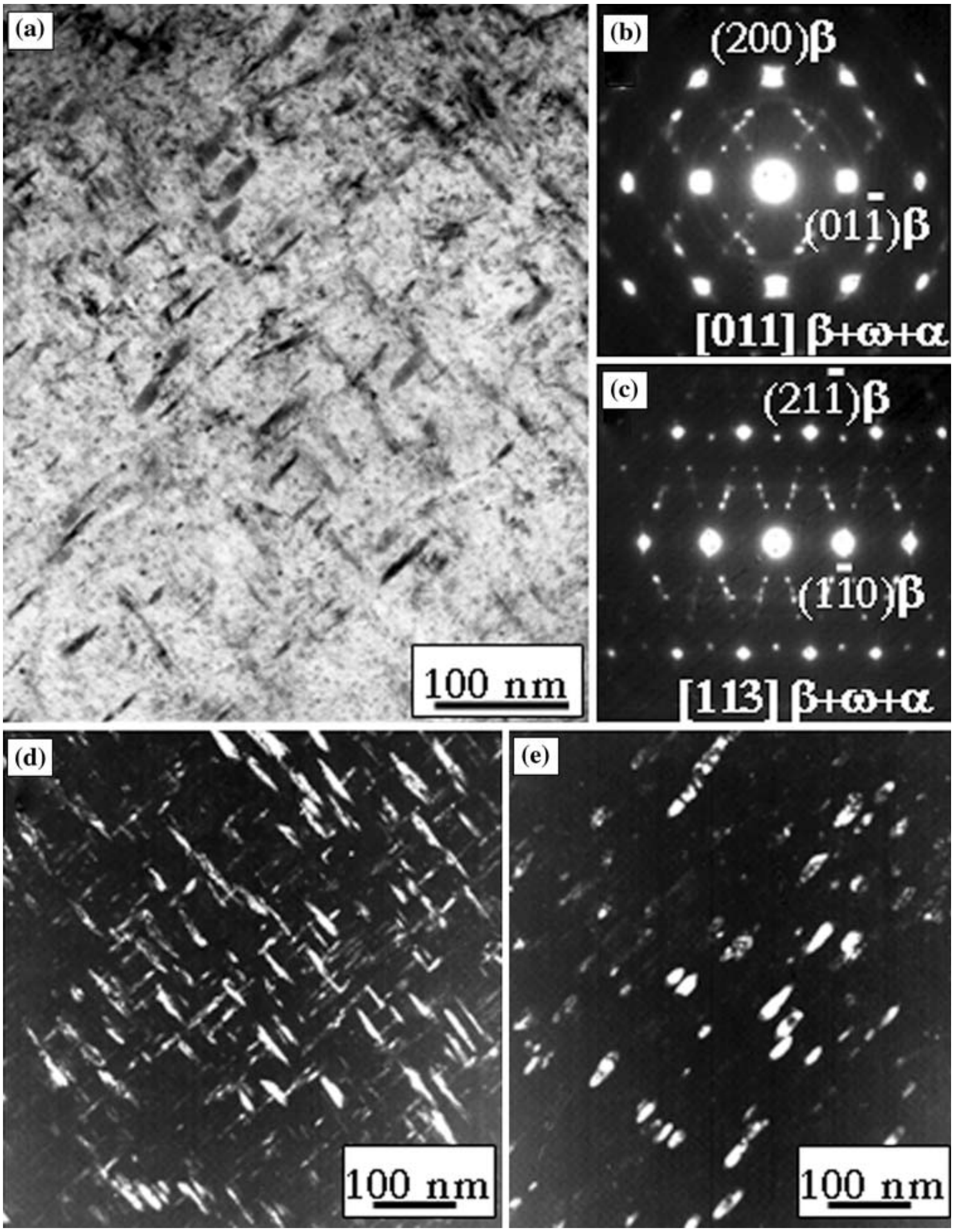

Fig. 3 **a** Bright-field TEM micrograph of TNZT alloy after β solutionizing/quenching/aging at 400 °C for 2 h, showing nanometer-scale second phase precipitates in addition to the β matrix phase. **b** [011]β zone axis SAD pattern from the matrix showing additional reflections that are visible at the 1/3 and 2/3 {112}β as well as at the 1/2 {112}β locations, corresponding to nanoscale ω and α precipitates, respectively. **c** [113]β zone axis SAD pattern from the matrix showing the same additional spots. **d** Dark-field TEM image recorded from one of the α-reflections at a 1/2 {112}β type position, showing an acicular morphology of α precipitates. **e** Dark-field TEM image recorded from one of the ω-reflections at a 1/3 {112}β type position, showing lenticular-shaped ω precipitates

the α and ω precipitates is likely to be due to the nucleation of the thermodynamically stable α precipitates, replacing the thermodynamically metastable ω precipitates which presumably act as heterogeneous nucleation sites. There have been previous reports in the literature of such ω-mediated nucleation of α in the β phase of titanium alloys [11, 17]. The proposed mechanism underlying such a nucleation process is that the metastable ω precipitates lead to highly localized coherency strains within the β phase and on subsequent annealing these strain centers act as potent nucleation sites with the α precipitates nucleating at ω/β interfaces [18, 19]. It must be noted that there is still some controversy in the literature regarding whether the α precipitates nucleate at the ω/β interfaces, or within the ω precipitates, or whether the ω precipitates undergo a solid-state transformation to form the α precipitates [10, 11, 17–21].

Compositional analysis of the 400 °C annealed TNZT sample was carried out using 3DAP tomography. A 3D reconstruction of the Ti (gray), Nb (red), Zr (blue), and, Ta (yellow) ions (colors seen only in online version) within a volume of dimensions 67 × 67 × 51 nm^3 are shown in Fig. 5a. While there is a semblance of compositional inhomogeneities in this 3D ionic reconstruction, a better representation of the compositional variations are the iso-concentration surfaces (or isosurfaces in short), that show the regions of enrichment (or depletion) for a specific alloying element. Such isosurfaces are shown in Fig. 5b–d.

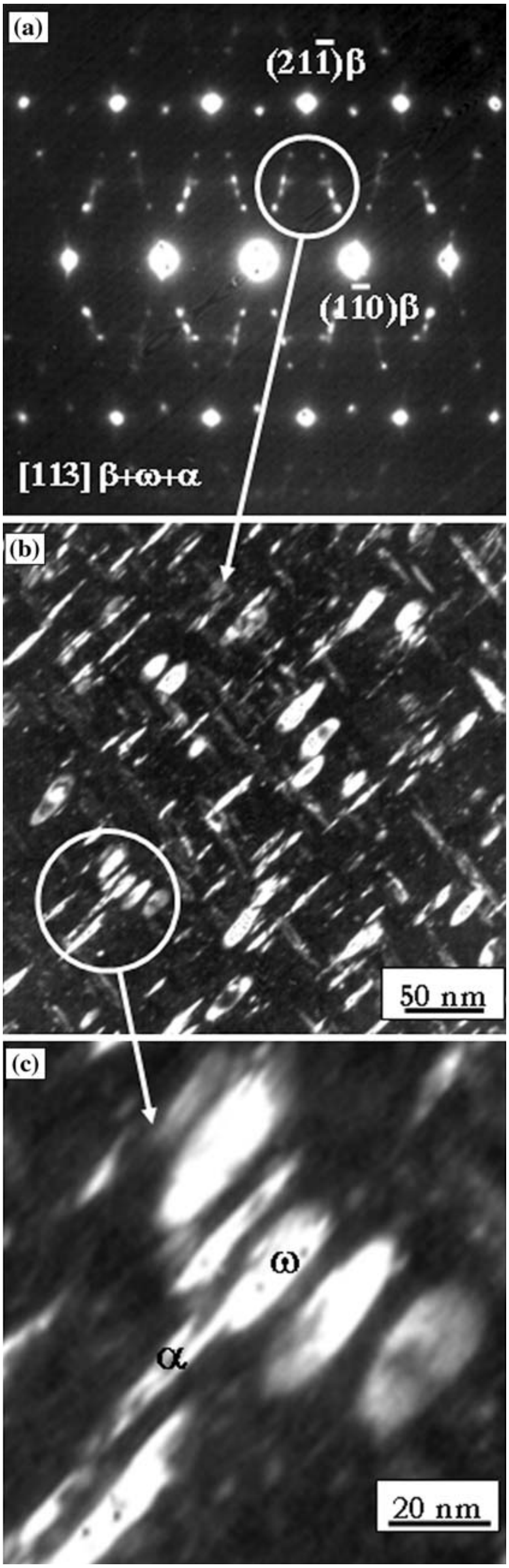

◀ **Fig. 4** **a** The same $[113]\beta$ zone axis SAD pattern as shown in Fig. 3c circling the reflections that were used to obtain a dark-field TEM micrograph. **b** The corresponding dark-field micrograph, with the α and ω precipitates that were imaged simultaneously. **c** A magnified view of one such region where an acicular α precipitate appears to be attached to a lenticular ω precipitate. The corresponding region is marked in (**b**)

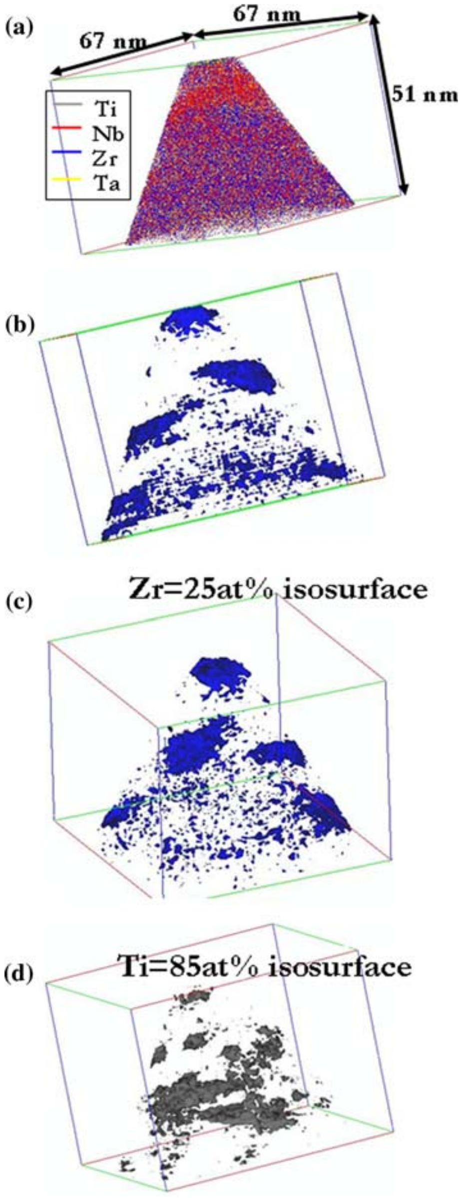

Fig. 5 **a** A 3D reconstruction of the 400 °C annealed TNZT sample analyzed using a LEAP^{TM} microscope, showing the Ti (gray), Nb (red), Zr (blue), and, Ta (yellow) ions (colors seen only in online version). **b** and **c** Zr isosurfaces of 25 at.% concentration (in blue) showing the α regions. **d** Ti isosurface of 85 at.% concentration (in gray) showing the ω regions

While Fig. 5b, c show Zr isosurfaces of 25 at.% concentration (in blue), Fig. 5d shows a Ti isosurface with a concentration of 85 at.% (in gray). Both the Zr and Ti isosurface renditions appear to depict Zr and Ti-rich precipitates in this sample though the identity of these precipitates is difficult to determine without a more detailed analysis of the actual composition profiles across these different types of precipitates as shown in Fig. 6. Figure 6a shows the 3D reconstruction of the same sample with both Zr and Ti isosurfaces plotted simultaneously. The composition profiles for Ti, Nb, and, Zr, across a cylinder of diameter 5 nm (marked in Fig. 6a) are shown in Fig. 6b. This composition cylinder intersects one of the Zr-rich precipitates (blue isosurface) as clearly visible in Fig. 6a. However, due to the perspective of Fig. 6a, it is difficult to visualize the entire 3D morphology. A different perspective view of the same reconstruction is shown in Fig. 6c with the same Zr-rich precipitate marked by a dotted arrow. In this view it can be clearly seen that the Zr-rich precipitate is associated with a Ti-rich precipitate (gray isosurface). The composition profile for this set of precipitates, shown in Fig. 6b, indicates that the Zr-rich region corresponds to an α precipitate while the Ti-rich region corresponds to an ω precipitate. This can be deduced based on the fact that both Nb and Zr destabilize the ω phase in titanium alloys [16], and therefore during isothermal annealing at 400 °C, it is expected that the growing ω precipitates will reject these two alloying elements leading to a local pile up of Zr and Nb adjacent to these precipitates. Since Zr is a marginal α stabilizer (relatively neutral element) while Nb is a de-stabilizer as far as α phase stability is concerned, the Zr-rich regions adjacent to the ω precipitates can nucleate α precipitates which tend to reject Nb as observed in the atom probe compositional profiles (Fig. 6b). Therefore, the α precipitate lies adjacent to the ω precipitate and are in contact with it. A second set of composition profiles for the same elements, corresponding to a different averaging cylinder of 5 nm diameter (marked in Fig. 6c), is shown in Fig. 6d. In these profiles too composition regions corresponding to both ω and α precipitates are visible. One of the regions corresponding to a ω precipitate (5.5 nm mark to 12.5 nm mark in Fig. 6d) possibly has an α precipitate (2 nm mark to 5.5 nm mark in Fig. 6d) lying adjacent to it (located right at the top of the 3D reconstruction in Fig. 6c). The other two Ti-rich regions, are likely to correspond to smaller ω precipitates exhibiting marginal variations in composition with respect to the adjoining β matrix. These smaller ω precipitates do not appear to act as α nucleation sites.

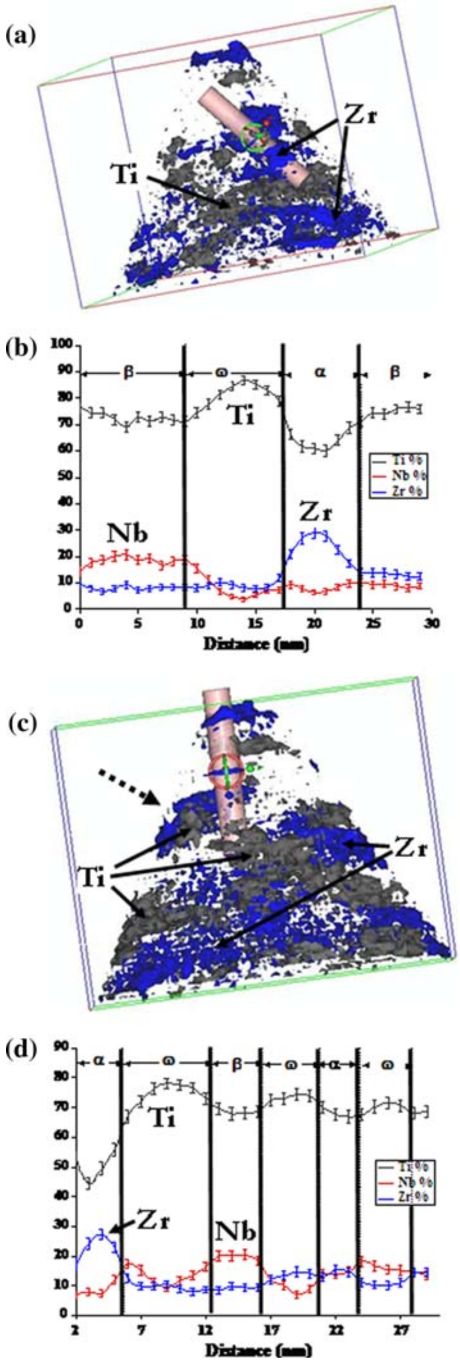

Fig. 6 **a** The same 3D reconstruction as in Fig. 5, showing the Zr (of 25 at.% concentration) and Ti (of 85 at.% concentration) isosurfaces plotted simultaneously. **b** The composition profiles for Ti (gray), Nb (red), and, Zr (blue), across a cylinder of diameter 5 nm (marked in **a**). **c** A different perspective view of the same reconstruction as in (**a**). The dotted arrow marks a particular region of interest that was analyzed via the compositional cylinder in (**a** and **b**). **d** The composition profiles for Ti (gray), Nb (red), and, Zr (blue), across a cylinder of diameter 5 nm (marked in **c**)

Based on this compositional analysis it is now possible to re-visit the 3D isosurface depictions for the individual Zr-rich and Ti-rich regions, shown in Fig. 5. Thus, while the Zr-rich regions in Fig. 5b, c correspond to α precipitates, the Ti-rich regions shown in Fig. 5d correspond to ω precipitates. Interestingly, the α precipitates, shown in Fig. 5b, c, exhibit a more plate-like (or lath-like) morphology in these 3D reconstructions as compared with the more acicular-like appearance in the 2D dark-field TEM image shown in Fig. 3d. Furthermore, it should be noted that the acicular α precipitates appeared to be marginally longer in the TEM images (∼20–50 nm in length) as compared with the 3D isosurface renditions. This is likely to be a consequence of the overlap of multiple α precipitates (or sections of these precipitates) in the 2D views of the TEM images. On comparing the TEM dark-field image of the ω precipitates shown in Fig. 3e with the 3D isosurface rendition shown in Fig. 5d, it appears that these precipitates are predominantly ellipsoidal in shape. Furthermore, based on the 3D isosurface rendition shown in Fig. 5d it appears that there is a range of sizes of these precipitates. It should be noted that the rather high density of ω precipitates present in this alloy impedes discerning individual precipitates in some cases due to substantial overlaps, as observed in Fig. 5d.

Summary

Laser-deposited Ti-34%Nb-7%Zr-7%Ta (wt%), after β solutionizing and quenching to room temperature, exhibits a microstructure consisting primarily of β grains with homogeneously distributed nanometer-scale precipitates of ω. These ω precipitates are in their early stages of development and consequently exhibit only limited rejection of alloying additions such as Nb. Solution treatment of this alloy (above the β transus temperature) and subsequent aging at 400 °C for 2 h leads to coarsening of the ω precipitates and substantial rejection of Zr and Nb (both ω de-stabilizers), measured using 3DAP tomography. Furthermore, these ω precipitates act as nucleation sites for α precipitates in this alloy as confirmed from detailed TEM studies. In addition to effects of coherency strains, the local enrichment of Zr adjacent to a growing ω precipitate appears to aid in the nucleation of α. These results demonstrate that coupling of TEM studies with 3DAP tomography can be very useful in investigating the early stages of precipitation of both metastable and equilibrium phases in these alloy systems.

Acknowledgements This work has been supported in part by the U. S. Air Force Office of Scientific Research (AFOSR), the National Science Foundation (NSF), and, the Center for the Accelerated Maturation of Materials (CAMM) at the Ohio State University.

References

1. Long MJ, Rack HJ (1998) Biomaterials 19:1621
2. Wang K (1996) Mater Sci Eng A213:134
3. Qazi JI, Marquardt B, Rack HJ (2004) JOM 56(11):49
4. Niinomi M, Hanawa T, Narushima T (2005) JOM 57(4):18
5. Keicher DM, Smugeresky JE (1997) JOM 49(5):51
6. Banerjee R, Nag S, Samuel S, Fraser HL (2006) J Biomed Mater Res 78A(2):298
7. Samuel S, Nag S, Scharf T, Banerjee R (2008) MSE-C 28(3):414
8. Banerjee R, Nag S, Fraser HL (2005) MSE-C 25(3):282
9. Duerig TW, Williams JC (1984) Beta Titanium alloys in the 80’s: proceedings of the symposium. Atlanta, GA, United States, pp 19–67
10. Blackburn MJ, Williams JC (1968) Trans Met Soc AIME 242:2461
11. Pennock GM, Flower HM, West DRF (1980) Titanium ‘80: science and technology, pp 1343–1351
12. Ohmori Y, Ogo T, Nakai K, Kobayashi S (2001) Mater Sci Eng A 312:182
13. Thompson K, Lawrence D, Larson DJ, Olson JD, Kelly TF, Gorman B (2007) Ultramicroscopy 107:131
14. DeFontaine D, Paton NE, Williams JC (1971) Acta Mater 19:1153
15. Banerjee R, Collins PC, Bhattacharyya D, Banerjee S, Fraser HL (2003) Acta Mater 51(11):3277
16. Williams JC, Hickman BS, Leslie DH (1971) Metall Trans 2:477
17. Furuhara T, Maki T, Makino T (2001) J Mater Proc Technol 117:318
18. Hickman BS (1968) J Inst Met 96:330
19. Langmayr F, Fratzl P, Vogl G (1994) Phys Rev B 49–17:11759
20. Azimzadeh S, Rack HJ (1998) Metall Mater Trans A 29:2455
21. Prima F, Vermaut P, Texier G, Ansel D, Gloriant T (2006) Scripta Mater 54:645